Original Article

Structural and Optical Properties Correlated with the Morphology of Gold Nanoparticles Embedded in Synthetic Sapphire: A Microscopy Study

María Luisa García-Betancourt, Carlos Magaña-Zavala, Alejandro Crespo-Sosa

Department of Experimental Physics, Institute of Physics, National Autonomous University of Mexico (UNAM), CDMX, Mexico

Abstract

This work reports on the electron microscopy analysis of the structure and morphology of gold nanoparticles produced by ion implantation as well as their relationship to their optical properties. Metalic nanoparticles by ion implantation are usually spherical and formed beneath the surface of a dielectric matrix. In this experiment, the matrix was sapphire. After high-energy Si ion irradiation, the gold nanoparticles were elongated into prolate spheroids. Since the nanoparticles are embedded in a dielectric matrix, secondary electron imaging in a JEOL JSM-7800F at low voltage did not allow their analysis. This work proposes an analysis using backscattered electron imaging in a field emission scanning electron microscopy at higher voltages (20 kV) to explore the morphology of the embedded nanoparticles. The samples were observed by cross-sectional view as well as a top view of the surface of the sapphire matrix for exploration and recognition of their morphology, dimensions, distribution, and composition. The analysis was extended by means of Rutherford backscattering spectrometry, X-ray diffraction, and optical extinction spectroscopy. The nanoparticles exhibited structural and optical properties correlated directly to the morphology observed by microscopy. The beam interaction with the sample and the used parameters was simulated in the CASINO code, from which the depth of exploration with distinct parameters used in microscopy analysis was estimated.

Keywords: Field emission scanning electron microscopy, microscopy, backscattered electrons, gold nanoparticles, ion implantation

Introduction

Nanomaterials are recognized as structures whose dimensions are within the range of 100 nm or less. Characterization is essential to understand the properties of any specimen containing nanostructures. The scanning electron microscopy (SEM) has become a fundamental tool in the development of nanotechnology over the last decades. Similarly, advances in nanotechnology have also improved the SEM components enabling observations at better resolution of nanostructures with nanometer dimensions,[1] which allow a better characterization. The wide range of SEM applications and fields for characterization include coatings,[2,3] earth sciences,[4,5] energy, fuel production,[6,7] nanomedicine,[8] and optoelectronics,[9] among others.

Nevertheless, not all specimens are good candidates for SEM characterization. In particular, those specimens produced by ion implantation in a dielectric matrix require special consideration. In previous research, SEM analysis was limited to show a bright line near the surface, which would correspond to the implanted region.[10] Other authors only reported the damage on the surface of implanted samples with various types of matrices.[11-13] Metallic nanoparticles (MNPs) embedded in dielectric matrixes have also been observed by high-resolution transmission electron microscopy (HRTEM). For example, Eichelbaum *et al*. reported the analysis of thin glassy silicate–titanate films in a cross-section view by HRTEM but exhibited the surface by SEM.[14] Sharp *et al*. showed a cross-section view of germanium nanocrystals

Access this article online

Quick Response Code:

Website: http://www.jmau.org/

DOI: 10.4103/JMAU.JMAU_19_18

Address for correspondence: Dr. María Luisa García-Betancourt, Center of Chemical Research-IICBA, Autonomous University of State of Morelos, Avenida Universidad 1001, Chamilpa, Cuernavaca, Morelos. E-mail: mluisa.garcia@uaem.mx

How to cite this article: García-Betancourt ML, Magaña-Zavala C, Crespo-Sosa A. Structural and optical properties correlated with the morphology of gold nanoparticles embedded in synthetic sapphire: A microscopy study. J Microsc Ultrastruct 2018;6:72-82.

embedded in sapphire.[15] More recently iron,[16] platinum,[17] or silicon[18] nanoparticles have been reported and characterized by HRTEM. However, the preparation of sample specimens produced by ion implantation for TEM analysis is destructive, arduous, and time-consuming during the thinning process of the matrix. In addition, one micrograph cannot represent the variety of sizes, shapes, and morphologies of the nanoparticles formed within one implanted sample. Therefore, there is a need to explore some other optional microscopy methods, which allow us to investigate the samples produced by ion implantation using only a thin portion from the sample. Fortunately, modern scanning electron microscopes and appliances open up the possibility of exploring these types of specimens, and hence, they reduce the preparation time.

In this work, the microscopy analysis of spherical and deformed gold nanoparticles (GNPs) embedded in a sapphire matrix was carried out using a JEOL JSM-7800F. SEM analysis has not usually been employed as characterization technique for MNPs synthesized by the ion implantation method due to the difficulty in that the MNPs are not on the surface; rather, they are encapsulated in a dielectric matrix. However, here, the observation of nanoparticles produced by the ion implantation methodology is proposed using mainly backscattered electron (BSE) imaging. The structure and optical properties of metal nanoparticles were also investigated using X-ray diffraction (XRD) and optical extinction, both of which are nondestructive techniques, to study the crystallography and absorption of the whole sample. While this methodology cannot replace the high-resolution analysis of implanted samples, it does offer a nondestructive, suitable, and cheaper alternative and complementary route for microscopy analysis when available.

Experimental Method

The samples were prepared by the ion implantation method, similar to that described in Sánchez-Dena *et al.* and Mota-Santiago *et al.*,[19,20] by which GNPs embedded in sapphire were produced. The ion implantation method consists of (i) ion implantation, (ii) annealing, and (iii) nanoparticle deformation. The scheme for the sample preparation is exhibited in Figure 1. Three gold ion implantations in sapphire (α-Al_2O_3 bought from Guild Optical Associates, Inc.) were performed at room temperature, at an 8° off-axis inclination to avoid channeling effects and using three different ion energies of 2.0, 1.5, and 1.0 MeV, successively [Figure 1a]. The fluences for each implantation were 7.52×10^{16} ions/cm^2, 7.52×10^{16} ions/cm^2, and 7.26×10^{16} ions/cm^2, respectively, with a current of 1 μA. After Au implantation, the samples were annealed at a temperature of 950°C, for 30 min in a reduced atmosphere of 50% H_2 + 50% N_2 [Figure 1b]. The deformation was carried out by subsequent Si ion irradiation, at an incidence angle of 75° and energy of 12 MeV [Figure 1c]. The current was measured at 1 μA in the sample holder, and the ion fluence was set to 2.34×10^{16} ions/cm^2, as measured by the integrated current.

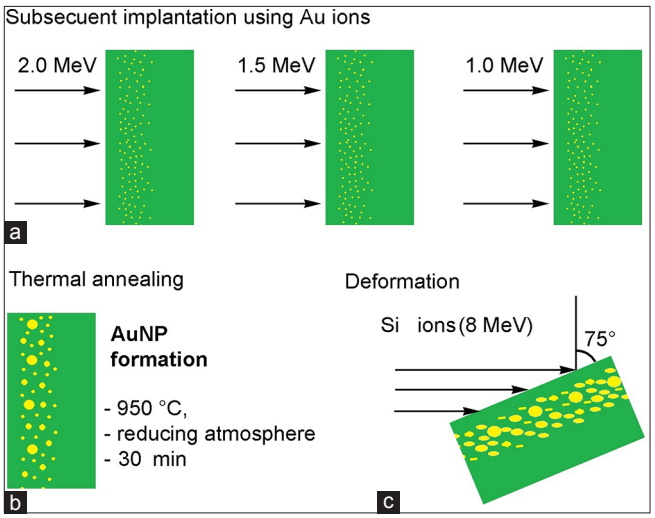

Figure 1: Formation and deformation schemes of gold nanoparticles embedded in a sapphire matrix. (a) Subsequent implantation using three Au ions in the following order: 2.0, 1.5, and 1.0 MeV. (b) Thermal annealing at 950°C in a reduced atmosphere for gold nanoparticle formation at different times: 15, 30, 60 and 90 min. (c) Deformation of gold nanoparticles using Si ions with a tilde of sapphire matrix at an angle of 75°

The characterization was achieved by JEOL Field Emission Scanning Electron Microscope JSM-7800F. For the purpose of this investigation, the methodology for dielectric sample preparation is displayed schematically in Supplementary Information Figure SI1: (a) First, a thin layer (thickness 200–300 μm) was cut from the dielectric sample, which contained the MNPs. (b) Next, the thin slice was placed onto the sample holder and attached by carbon tape. Most of the unimplanted dielectric region was covered with carbon ink, ensuring a good electrical contact with the sample holder, but leaving the implanted region uncovered. (c) Finally, the sample was carbon coated in an Ernest F. Fullam, Inc., carbon evaporator with three instant sparks to reach a thin layer of around 15–20 nm on the top. For the analysis of the nanoparticles on the surface, Step 1 [Supplementary Information Figure SI1a] was distinct; the surface was polished and placed directly on the sample holder for FE-SEM [Supplementary Information Figure SI1b] and carbon coated as shown in Supplementary Information Figure SI1c.

The specimens contained high-Z MNPs embedded in a low-Z dielectric matrix, and to characterize the sample, we needed to use an FE-SEM in BSE imaging, gentle beam (GB), and cryo-transfer system modes. In fact, these options are employed for different kinds of sample characterizations: GB mode was used because it gives a charge balance and extremely high-resolution imaging in dielectric samples.[1] Although the cryo system is widely used for frozen samples, it is also an option for better stabilization of a dielectric sample. The cryo-transfer system allows an extended working time on a specific region of the sample by dissipating the heat that is

1 http://www.jeolusa.com/RESOURCES/Electron-Optics/Documents-Downloads/EntryId/990

generated in the sample by the electron beam.[2,3] The operational conditions are specified as follows: work distance between 3 and 6 mm, 20 kV of acceleration voltage, 10 nm spot, and ~ 98 nA probe current. The beam diameter for this current was 12.6 nm; this value was estimated from the JEOL operating manual "SEM A to Z".[4] For the acceleration voltage, 20 kV was the most suitable for imaging using BSE in our sample, which contained MNPs in a dielectric matrix. The use of BSE requires a minimum acceleration voltage, as was previously suggested by Niedrig.[21]

The implanted samples were also characterized by Rutherford backscattering spectrometry (RBS) in a Pelletron facility with a 2.0 MeV He^+ beam, to determine the distribution of the implantation. Samples were also studied by XRD over the C-plane direction of the sapphire matrix (the C-plane is parallel to the surface of the sapphire) using a Bruker D8 Advance diffractometer with CuKα radiation (λ = 1.5406 Å). The diffractograms were recorded at room temperature in the 2θ range between 20° and 90°. Optical characterization was carried out in the transmission mode in the UV–Vis region with an Ocean Optics USB2000 spectrometer to study the localized surface plasmon resonance present in the extinction spectrum taking into account the correction from the contribution of the refractive index of sapphire (1.76). To measure the samples with deformed nanoparticles, the samples were placed and oriented parallel to the minor axis and polarized light was used.

The SRIM (http://www.srim.org/) and Casino Monte Carlo (http://www.gel.usherbrooke.ca/casino/) codes were used to simulate the interaction of radiation with sapphire. SRIM estimated the implantation depth of Au ions into the sapphire matrix and compared with the experimental results. CASINO simulated the penetration of electrons into sapphire containing gold layers.

Results and Discussion

Backscattered electron imaging for spherical gold nanoparticles

The JEOL JSM-7800F FE-SEM has specific characteristics and multiple components for different analyses; these components include a backscattered electrons detector. The BSEs are incident electrons that come back out of a target and are imaged with the scanning electron microscope.[22] This method is particularly suitable for the characterization of composite samples formed by elements with markedly different Z atomic numbers. The image is formed in the SEM through different contrasts; while the Z increases, the number of BSEs also increases.[23]

Figure 2a displays a typical micrograph from the matrix containing embedded MNPs in a transversal view, captured by scanning BSEs. This kind of image shows distinct contrasts for distinct atomic numbers; Au has an atomic number $Z = 79$, which is considerably higher than the matrix elements of Al_2O_3, $Z = 13$ (aluminum) and $Z = 8$ (oxygen). Consequently, GNPs appear more brilliant than the matrix. The Z-contrast in nanoparticles can be enhanced using the inverse mode, as shown in Figure 2b. Both micrographs were captured at a magnification of ×100,000. Such micrographs exhibit GNPs after thermal annealing. A similar surface was previously observed without any carbon layer [Supplementary Information Figure SI2], allowing an estimation that the implantation zone, where nanoparticles are formed, begins ~ 110 nm distance from the surface.

Valuable information was recovered from the micrographs, which shows the implantation zone after thermal annealing. The line in magenta color, drawn in Figure 2a, indicates a line profile illumination carried out by the image processing program, Image-Pro Plus software (http://www.mediacy.com/imageproplus), of the transversal view of the implantation zone. The line profile records the intensity of illumination for any image. The illumination line profile has been applied previously to appreciate and differentiate metals with diverse Z numbers.[24,25] Diverse lines (30) are measured at the same height along the micrograph and then averaged. Figure 2c shows a plot for the average of these 30 line profiles over the micrograph as exhibited in Figure 2a. This information gives qualitative information about the gold content and its distribution in the implantation zone beneath the surface. However, the gold content can be estimated by the RBS spectrum performed over the sample before annealing, depicted in the plot of Figure 2d, where the signal peak of the implanted gold ions can be observed between the 400–600 channels. The gold content in atomic percentages was calculated from the RBS spectrum as a function of depth [Figure 2e]. The estimated number of ions that were implanted in the sapphire from this plot was 5.58×10^{16} ions/cm^2.

The line profile from Figure 2c measured from the micrograph can be correlated to the RBS spectrum and the atomic percentage of gold, by means of a deconvolution into three Gaussian plots. The maximum values of each Gaussian give information about the depth position of each implantation. The values for depth for RBS are similar to the ones observed for the line profile [Figure 2c], but differences could be attributed to thermal annealing, which was carried out for 30 min. The values for the gold concentration in the sapphire matrix were esimated for each energy using the SRIM[26] program: the depth implantation values were 146 nm for implanted ions of 1 MeV, 208 nm for 1.5 MeV, and 272 nm for 2 MeV. The quantities we observed were quite different for several reasons from the ones calculated using SRIM: (i) maybe the ions were removed during the subsequent ion implantation and (ii) the gold distribution changed due to the presence of nanoparticles

2 https://www.jeolusa.com/DesktopModules/Bring2mind/DMX/Download.aspx?EntryId=710&Command=Core_Download&language=en-US&PortalId=2&TabId=320.

3 JSM-7800F Schottky Field Emission Scanning Electron Microscope https://www.jeol.co.jp/en/products/detail/JSM-7800F.html

4 Scanning Electron Microscopy A to Z. Basic Knowledge for Using the SEM. https://www.jeol.co.jp/en/applications/pdf/sm/sem_atoz_all.pdf

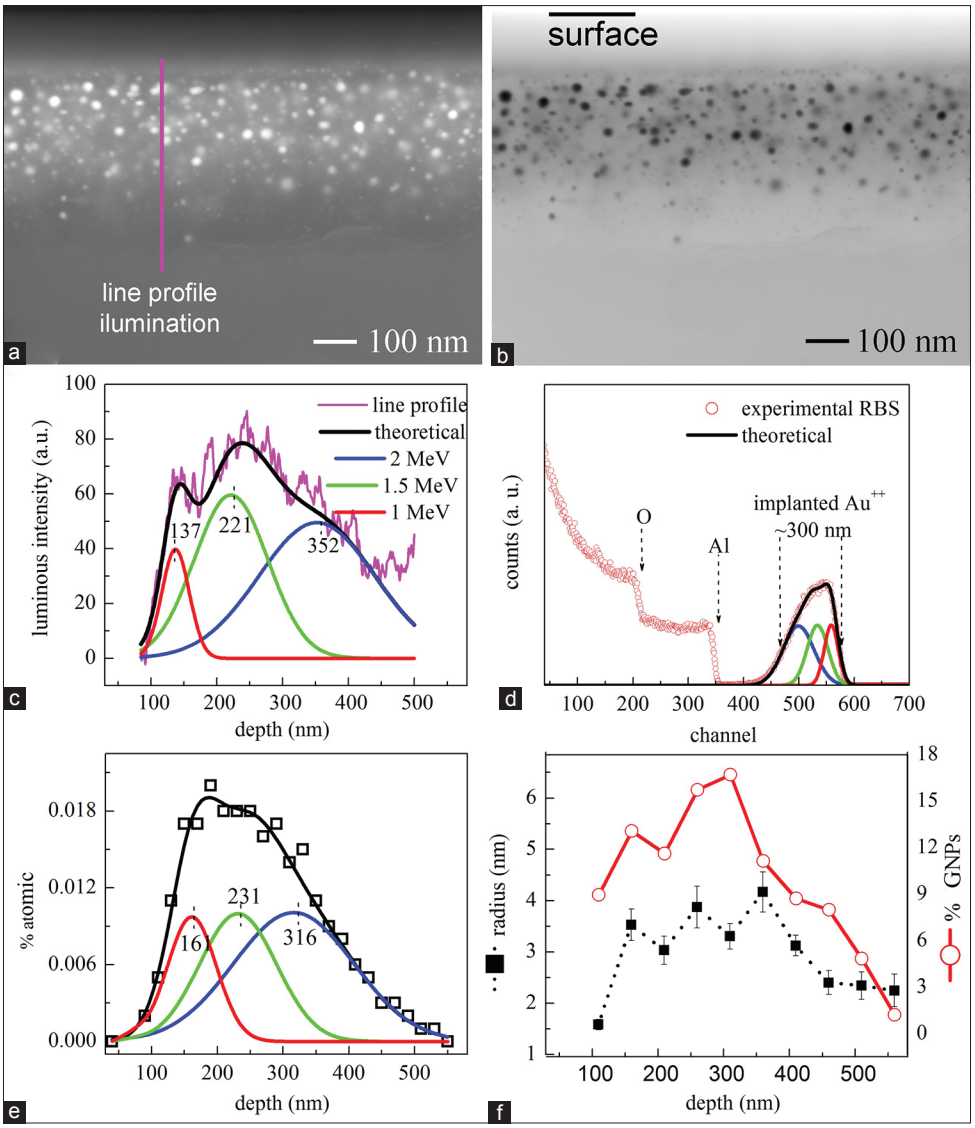

Figure 2: (a and b) Typical field emission scanning electron microscopy micrograph of metallic nanoparticles embedded in a matrix observed in a transversal view. (c) Average line profile of intensity at long ion implantation observed in field emission scanning electron microscopy micrograph and decomposed into three Gaussian distributions. (d) Plot from Rutherford backscattering spectrometry. (e) Gold content as a function of depth. (f) Plots for the radius and the percentage of gold nanoparticles as a function of the depth

formed after annealing of the sample. When comparing the ion distribution seen by RBS with the results from microscopy techniques, we find a good agreement for the GNP distribution for a large portion of the surface sample.

The size and percentage of MNPs can also be estimated as a function of depth from the FE-SEM micrograph [Figure 2a], which was divided into 50 nm slabs throughout the implantation zone. Figure 2f depicts the plots for the radius versus the percentage of GNPs as a function of depth measured from the surface. The GNPs were measured and counted in a section of the micrograph. As can be noted, the plots for radius and percentage of nanoparticles versus depth exhibit behaviors similar to the line profile [Figure 2c] and the gold content [exhibited in Figure 2e]. Despite the wide size distribution of nanoparticles synthesized by the ion implantation method, the measured radius averages are of the same order when the depths are measured at 150–400 nm intervals, indicating a consistency in the dimensions of the nanoparticles formed in the main implantation zone. However, the percentage of nanoparticles (% GNPs) within the same region increases due to the contribution of small nanoparticles to the statistics. This effect is also notable in the increment of error bars for average sizes of the radii at some points from an interval, indicating at this position that the sample has more small nanoparticles.

Top view of the sample

Figure 3a shows an inverse BSE micrograph for the top view of the sample exhibited and studied as shown in Figure 2. The micrograph in Figure 3a was performed after polishing the surface, to reach the nanoparticles, and following Step 2 and Step 3 for the sample preparation [Supplementary Information

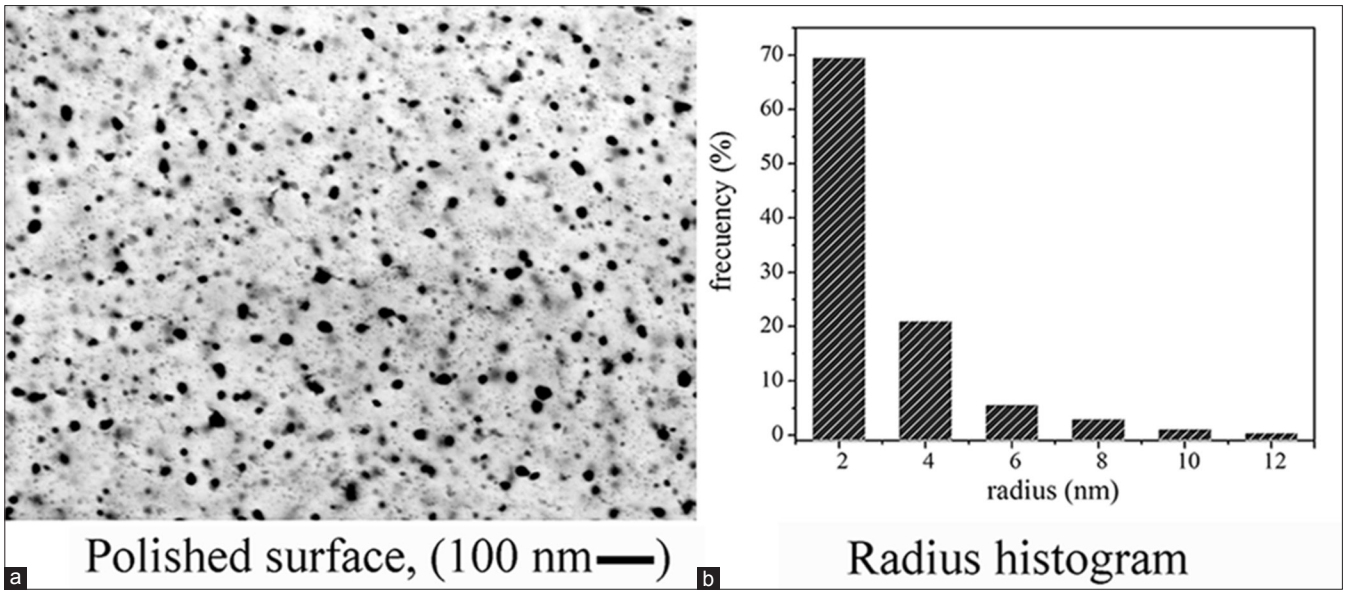

Figure 3: (a) Top view of the gold nanoparticles embedded in the sapphire matrix and formed after 30 min of annealing. (b) Histogram of the radius for gold nanoparticles

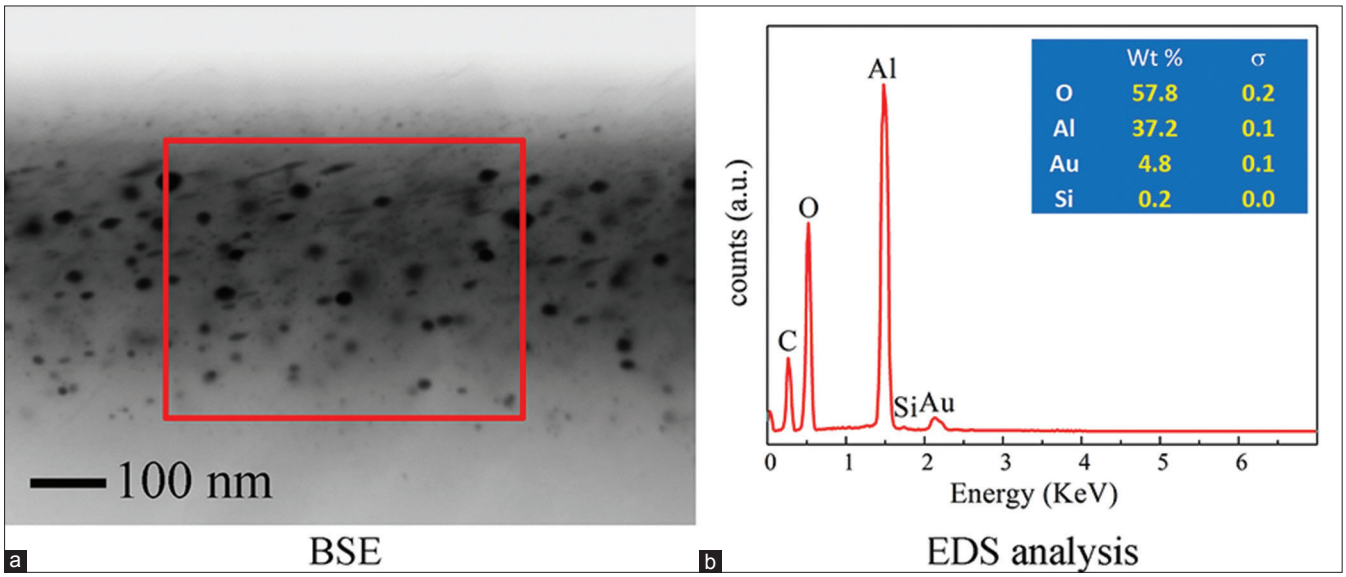

Figure 4: (a) Backscattered electron micrograph for deformed nanoparticles observed by a transversal view including a red square for (b) energy dispersive X-ray spectrum analysis

Figure SI1]. A diameter histogram of Figure 3b shows the tendency in the dimensions of GNPs formed after 30 min of annealing. This tendency demonstrates a preferential formation of small nanoparticles around 2 nm in radius. An average radius of 3.2 ± 0.1 nm was measured over 300 NPs, but a standard deviation of ~40% was observed, indicating a dispersion in the variety of radii, where the minimum and maximum values were 1.86 nm and 11.21 nm, respectively. The average indicates that the sapphire was removed by polishing at about 150 nm and 350 nm as can be confirmed by the plot for radius average as a function of depth [Figure 2f].

Deformation of gold nanoparticles and elemental analysis

Figure 4a displays scanning BSE micrographs for the edge of the sapphire matrix in transversal view with a magnification of ×200,000. With this micrograph, it was possible to observe the deformed nanoparticles with variable sizes and degrees of deformation as well. The sample described here corresponds to the nanoparticles deformed by Si ions. An elemental analysis of GNPs deformed by silicon irradiation was carried out on the implantation zone by energy dispersive X-ray spectrum (EDS) analysis [over the red square of Figure 4a]. Figure 4b exhibits the EDS for deformed GNPs from the area inside the red square as shown in Figure 4a. The corresponding X-ray emission peaks are labeled with each element in the sample; carbon was set in the software as a coating. The inset details the weight percentage of each element (O, Al, Au, and Si).

Morphology comparison and optical extinction

Higher magnification was performed to appreciate the morphology and size distribution of MNPs embedded in the sapphire matrix. Figure 5 shows BSE micrographs by inverse mode using a magnification of × 400,000. These micrographs correspond to the sample before [Figure 5a] and after [Figure 5b and c] deformation with Si ions and were captured at the same depth for each one (~200 nm). This magnification was enough to observe nanoparticles in some detail as well as the change in morphology between the as-annealed sample and the samples with deformed nanoparticles by means of postirradiation with Si ions in two views: Figure 5b side view and Figure 5c head-on view. As can be seen, the as-annealed sample exhibits, in general, nanoparticles with spherical morphology and a wide variety of diameters while the postirradiated samples contain embedded deformed nanoparticles with a prolate morphology, where the major axis resulted in an alignment with the direction of irradiation with the silicon ions (~15°) from the surface. Optical extinction spectra are shown in Figure 5d. While the original spectrum is strong and well defined for spherical nanoparticles, in the spectrum of the deformed nanoparticles after Si irradiation, the two resonances could be the effect on the polarization of light or the geometrical orientation of the sample in relation to the incident angle, which is distinguished with the proper alignment and polarization to the light used to analyze the sample. This effect has been previously found and explained in terms of the two normal oscillation modes of the electron clouds confined within the MNPs.[27-30]

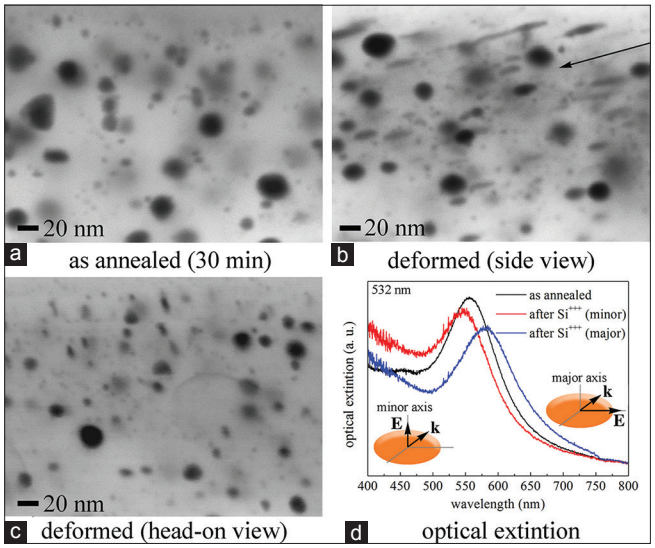

Figure 5: Morphology comparison between as-annealed and deformed gold nanoparticles using the same magnification in field emission scanning electron microscopy for backscattered electrons. (a) Implanted sample with gold nanoparticles annealed for 30 min in a reduced atmosphere. (b) Side view and (c) head-on view of deformed nanoparticles using a postirradiation with 12 MeV Si ions over spherical gold nanoparticles. (d) Optical extinction spectra of the same sample using polarized light, to selectively excite the resonant modes of the major or minor axis

The average size of the nanoparticles (as-annealed gold and deformed) was measured from several images similar to those displayed in Figure 5a and b. A total of 300 nanoparticles were measured in each case. The radius histogram for the as-annealed (for 30 min) ones is presented in Figure 6a, where

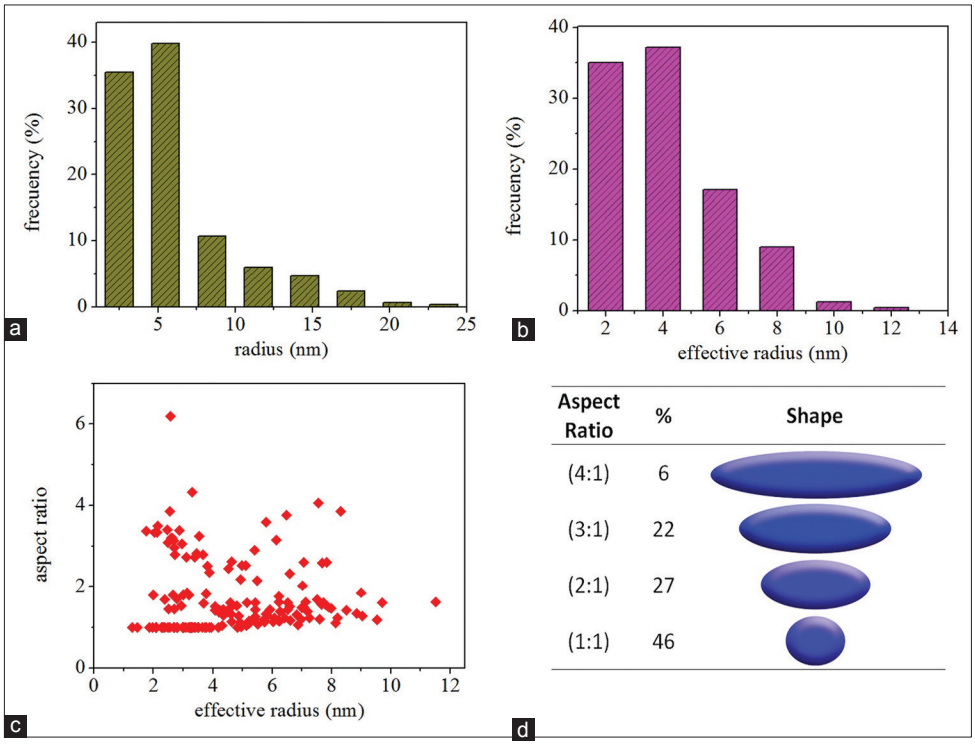

Figure 6: (a) Histogram for the radius of spherical gold nanoparticles. (b) Histogram for the effective radius of the deformed nanoparticles. (c) Aspect ratio versus effective radius. (d) Classification of nanoparticles with the aspect ratio

it can be seen that the predominant morphology was spherical and that the average radius was 5.58 ± 0.14 nm. Figure 6b shows the effective radius histogram of the deformed nanoparticles, where an average value of 6.11 ± 0.21 nm was found. The effective radius (r_{eff}) is defined as the radius of a sphere of the same volume ($\frac{3}{4}\pi a^2 c = \frac{3}{4}\pi r_{eff}^3$). Where a is the minor axis and c is the major axis of the prolate spheroid. Figure 6c shows the effective radius (r_{eff}) versus the aspect ratio (c/a). Figure 6d shows the percentage of the aspect ratio measured in deformed nanoparticles.

X-ray diffraction analysis

The crystal structure of the GNPs formed in the sapphire matrix was verified by means of XRD analysis. Figure 7a presents the diffractograms of both, i.e. the sample with nanoparticles before (a) and after (b) being deformed with Si ions. The composite sample formed by an α-Al_2O_3 monocrystal with embedded Au nanocrystals showed three main peaks; one of them is Sharp and located at 2θ = 41.7° that corresponds to the (0006) plane of the sapphire, measured in the C-direction [perpendicular to the C crystallographic plane of the sapphire, Figure 7b], while the peaks located in 2θ at 38.4° and 64.9° correspond to the (111) and (220) planes of the face-centered cubic (FCC) gold, represented in the schematic of Figure 7c.

In comparison with standards of power diffraction for FCC gold, the peaks that usually appear in 44.46° (200) and 77.45° (311) are not significantly present in the diffractograms of our samples. The first one (200) was marked in the diffractograms where it should appear. These facts could be attributed to the gold crystallites, which are homogeneously and preferentially oriented in the sapphire monocrystal. The ratios between the intensities of the (220) and the (111) peaks decreased after Si irradiation of the samples, 0.64 (before) and 0.29 (thereafter), suggesting an increment in the tendency of the (110) facet to be oriented parallel to the C-plane of the sapphire. The grain size and the lattice constant of the GNPs were calculated by peak indexing from d-spacing of the main peak. For the (111) peak of the as-annealed nanoparticles, the d-spacing was 2.34 Å, resulting in 5.31 nm and 4.04 Å as grain sizes and lattice constant, respectively. For deformed nanoparticles,

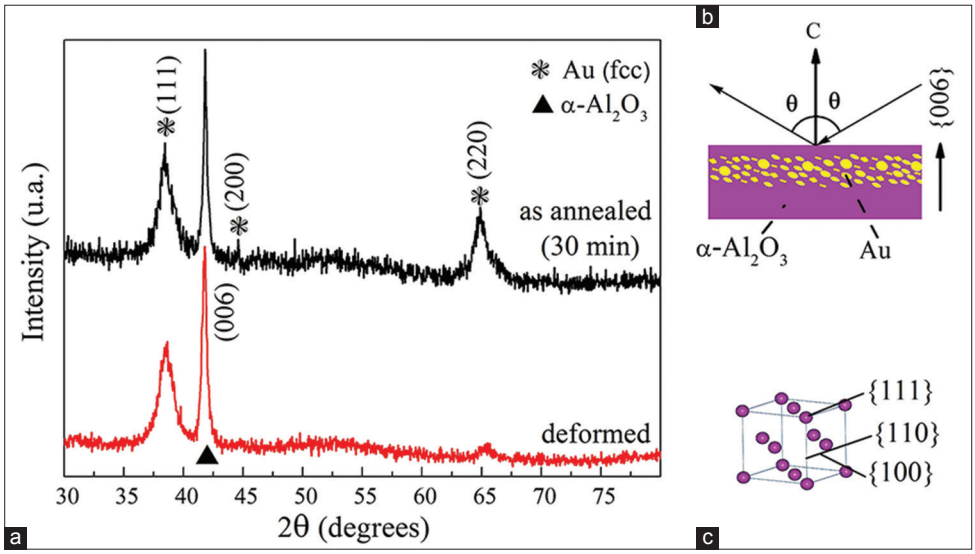

Figure 7: (a) X-ray diffractograms carried out over the composite formed by gold nanocrystals embedded in a sapphire matrix, (b) schematics for the measurement of diffractograms, (c) unit cell of gold

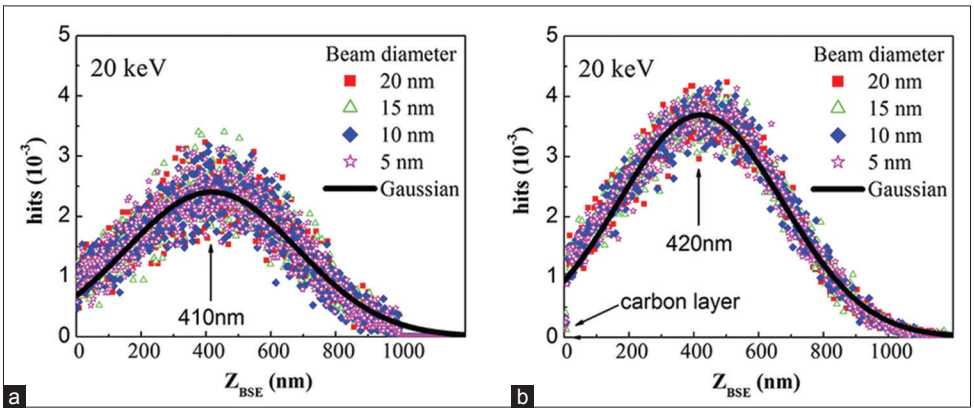

Figure 8: Monte Carlo simulation for electron beam interaction in (a) sapphire and (b) sapphire with a carbon coating of 10 nm

the d-spacing was 2.34 Å, resulting in 6.02 nm and 4.04 Å as grain sizes and lattice constant, respectively. The values are in agreement with the literature.[31,32] The grain sizes match the measured values for nanoparticles in micrographs from Figure 5 and histograms from Figure 6, indicating the fromation of nanometric crystaline monodomains. Similar d-spacings and lattice constants were measured from as-annealed and deformed nanoparticles, but a particle size difference was observed: deformed nanoparticles were slightly bigger than the as-annealed ones which may be due to the fact that the measurement was carried out over elongation (major axis).

Charge on the sapphire matrix

Scanning electron micrographs generated by SEs provide information about the surface of any specimen. SEs are usually generated by ionization of bound electrons or excitation of conduction electrons during the incidence of electrons, where energy is in the KeV range. They emerge chiefly from a thin layer some nanometers below the surface (~5 nm).[21,33] In the case of insulators containing embedded nanoparticles, such as those synthesized by ion implantation, it is difficult to obtain the relevant information about the morphology of the nanoparticles.

Furthermore, experimentally, a charge accumulation on the surface of the matrix occurred and precluded observation of the nanoparticles in the matrix by SEM characterization. Some difficulties regarding the dielectric nature of the matrix containing the MNPs were overcome in the proposed sample preparation before optimization. Most of the difficulties were due to charging of the sapphire: (i) the movement of the image while capturing the micrographs [Supplementary Information Figure SI3] involved solving this situation using the cryo system, implemented the carbon coating over a small fraction of sample, as proposed by our methodology. (ii) An effect noted in the resolution between the nanoparticles was solved using a thin fraction of the sample and increasing the acceleration voltage from 15 kV [Supplementary Information Figure SI4 for the entire sample] to 20 kV [Supplementary Information Figure SI5 for a thin layer of sample] for comparison. (iii) The total charging over the sapphire surface led to the observation of the inner part of the microscopy [Supplementary Information Figure SI6]. The mirror behavior of the sapphire was observed and solved by adding carbon ink at the edges with contact with the sample holder and next adding a carbon coating over the surface. (iv)

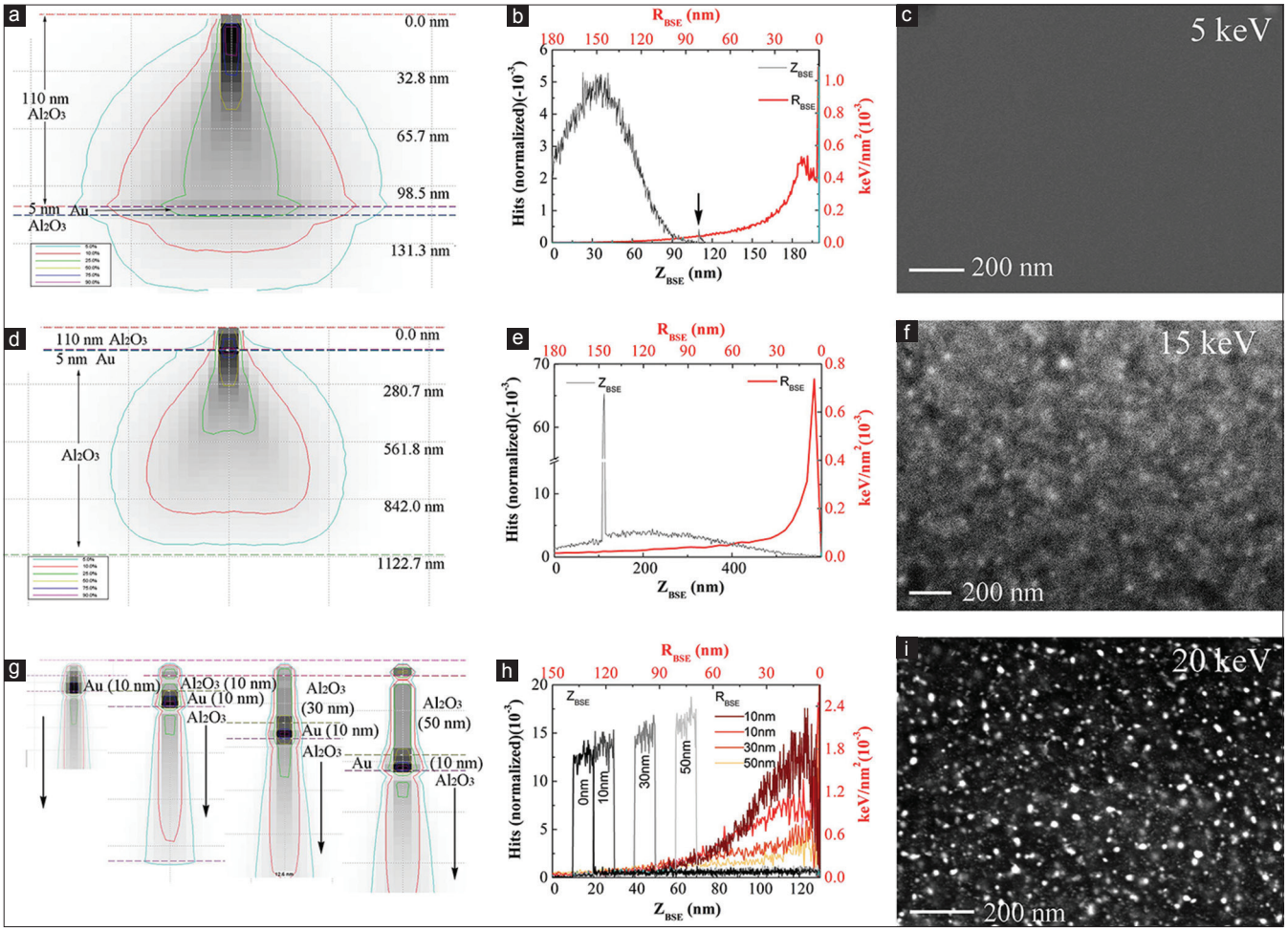

Figure 9: Monte Carlo simulation of electron beam interaction for layers of sapphire/gold/sapphire using (a-c) 5 keV and (d-f) 15 keV, and for (g-i) carbon/sapphire/gold/sapphire, varying the sapphire1 layer: 0, 10, 30 and 50 nm

Charging beneath the individual nanoparticles [Supplementary Information Figures SI7] was noted. We used the cryo system and stabilization around 1 h before characterization to help reduce this problem.

In general, carbon coating reduced the accumulation of charge on the sapphire surface and BSE allowed the analysis of MNPs. The BSE signal provided depth information, and this information was much better defined than the SEs because it essentially depends on imaging the scattering properties of the atoms which compose the solid and on the arrangement of the atoms within it.[21]

Monte Carlo simulation

A Monte Carlo simulation was carried out to study the electron–beam sample interactions that occur in SEM when using sapphire. The parameters employed in this work were as follows: the beam diameter was 12.6 nm and acceleration voltage was 20 keV. The results were compared with some experimental examples. The results were classified as follows:

The effect of the beam diameter and the carbon layer added to the sapphire at an acceleration voltage of 20 keV

Figure 8 exhibits the maximum penetration depth in the sample of (a) sapphire or (b) sapphire with a 10 nm carbon layer of electron trajectories that will escape to the surface (BSE). The plots simulated at 20 keV at distinct beam diameters (5, 10, 15, and 20 nm) exhibit Gaussian behavior. The variations in beam diameter and carbon layer do not imply a marked impact on the penetration depth of the electrons escaping from the sapphire surface. However, the addition of a carbon layer affects the trajectories and the number of electrons that penetrated the sapphire and will escape as BSE. For clean sapphire, the dispersion with respect to the Gaussian distribution is bigger; it implies that electrons have a variety of trajectories to follow, reducing the probability of achieving the maximum penetration in the material. When adding a carbon layer of ~10 nm, the dispersion is lower with respect to Gaussian distribution and the probability of having more electron heating and more information with BSE at a depth of 420 nm in sapphire is bigger than for clean sapphire.

Gold nanoparticle observations at different voltages and depth

Figure 9 displays the result of simulating an electron–sample interaction at different voltages and also for gold at different depths. Figure 9a-c presents the analysis for an acceleration voltage of 5 keV and a beam diameter of 12.6 nm for sample conditions with sapphire (110 nm), gold (5 nm), and sapphire (1000 nm) layers. The analysis in CASINO for these conditions provides an energy distribution, exhibited in Figure 9a, where the maximum value (black zone) did not reach the gold layer. Figure 9b shows a black plot for penetration (Z_{BSE}) of electrons that will be BSEs versus the number of hits normalized and a red plot for the radius of BSEs (R_{BSEs}) that will escape from the surface versus the energy density per nm^2. The maximum penetration of ~40 nm of electrons that will be backscattered is not enough to show information about gold embedded in the sapphire matrix. In addition, the maximum value of the radius for electrons escaping from the surface was ~11 nm, and a substantial amount of energy was lost; certainly, the electrons never reach the BSE detector, as exhibited by the micrograph in Figure 9c. That micrograph was captured at these conditions, at the surface of the sapphire which contained embedded GNPs where the implantation zone began at ~110 nm depth.

Figure 9d-f shows results of CASINO and SEM for an acceleration voltage of 15 keV and a beam diameter of 12.6 nm for the same sample conditions as those previously described. The energy distribution, exhibited in Figure 9d, achieves a maximum value (black zone) that reached the gold layer of 5 nm. Figure 9e shows the black plot for Z_{BSE}, where the maximum value of electrons that will be BSEs should be due to the gold layer, and most of the BSEs that escape from the sapphire surface will have a R_{BSE} distribution with a maximum value of ~5 nm, but it is possible that some BSEs reach the detector and form an image with low quality as shown at Figure 9f.

Figure 9g-i presents the analysis for the simulation of a specimen where a sapphire layer of ~110 nm was polished and used an acceleration voltage of 20 keV. The simulation was carried out using a layer of gold at different depths in sapphire: 0, 10, 30, and 50 nm. A 10 nm carbon layer was also added in order to perform a simulation similar to the experimental condition. Figure 9g shows the energy distribution for each case, where the maximum energy is mainly localized in the gold layer, independent of the sapphire thickness. This fact can also be appreciated by the Z_{BSE}, at distinct depths in Figure 9h, where most of the BSEs would come from the gold. However, not all the BSEs from the gold have an impact on the resulting micrograph, mainly because they are less energetic with short R_{BSE} and come from 30 and 50 nm of sapphire, so they should lose energy from the inelastic interaction with sapphire.

If any BSEs that escape from the surface contribute to the micrograph formation, then the area under R_{BSE} distribution can be correlated with the intensity of objects for any micrograph, as exhibited in Figure 9i. The area under R_{BSE} plot for 50 nm is almost 30% of the curve for 0 nm. The micrograph contains objects with a distinct bright intensity; however, the less intense has ~20% brightness with respect to the brightest. This then means it is possible that these parameters (20 keV acceleration voltage, 12.6 nm beam diameter, and carbon layer of 10 nm) could give information at a depth of 50-60.

Conclusions

This microscopy study by field emission scanning microscopy was carried out on sapphire samples containing embedded GNPs. We described in detail the best methodology to produce and observe spherical and prolate GNPs. The parameters we used were implemented in a CASINO simulation to estimate the achievements of our methodology. Despite the

adverse properties of the matrix, we managed to observe and characterize the GNPs with spherical and elongated morphologies as well as their dimensions, composition, and distribution near the surface. The distribution that was studied by line profile of the illumination in the micrographs was consistent with the implantation content profile measured by RBS. XRD studies confirmed the crystallinity of the GNPs formed in the sapphire matrix. The grain size calculated from indexation of the main peak (111) for FCC gold had good agreement with the values for GNP sizes measured from the FE-SEM images. In the case of elongated nanoparticles, the (220) peak of the diffractogram exhibited a decrease in intensity, indicating that the (110) facet of the FCC gold unit cell was reoriented during the deformation of the nanoparticles. The optical extinction spectra also revealed that optical properties are dependent on the morphology. In general, it can be concluded that the proposed methodology is a desirable route for characterization of MNPs embedded in a dielectric matrix, which can give relevant information, not always obtainable by other methods. From the CASINO simulation with our parameters, we established that information could be obtained from a depth of 50–60 nm.

It is important to mention that imaging of the deformed nanoparticles is also of fundamental scientific importance since it proves the formation of ion tracks in sapphire and therefore the feasibility of deformation of the nanoparticles, as we have reported previously for platinum nanoparticles embedded in sapphire and silicon matrix.[34] However, a discussion of the process is beyond the scope of this paper and will be discussed elsewhere in the future.

Acknowledgments

The authors gratefully acknowledge JEOL de Mexico S.A. de C.V., the Pelletron Accelerator, LAREC (Laboratorio de Refinamiento de Estructuras Cristalinas), and LCM (Laboratorio Central de Microscopía) at the Instituto de Física, Universidad Nacional Autónoma de México. For their technical support, the authors thank in particular L. Enriquez (JEOL), M. Palacios (JEOL), K. López Guzmán, F. Jaimes Beristein, M. Escobar-Reyes, A. Morales Espino, J.-G. Morales-Morales, D. Quiterio-Vargas, R. Hernández Reyes, and M. Monroy-Escamilla.

Supplementary Information

Supplementary information is available at Journal of Microscopy and Ultrastructure online (http://www.jmau.org/).

Financial support and sponsorship

This project was partially supported by DGAPA-UNAM (No. IN1081113). MLGB thanks CONACyT for their sponsorship (Grant No. 290847) to carry out this project.

Conflicts of interest

There are no conflicts of interest.

References

1. Suga M, Asahina S, Sakuda Y, Kazumori H, Nishiyama H, Nokuo T, *et al*. Recent progress in scanning electron microscopy for the characterization of fine structural details of nano materials. Progr Solid State Chem 2014;42:1-21.
2. Raulio M, Järn M, Ahola J, Peltonen J, Rosenholm JB, Tervakangas S, *et al*. Microbe repelling coated stainless steel analysed by field emission scanning electron microscopy and physicochemical methods. J Ind Microbiol Biotechnol 2008;35:751-60. DOI: 10.1007/s10295-008-0343-8.
3. Dahlström C, Allem R, Uesaka T. New method for characterizing paper coating structures using argon ion beam milling and field emission scanning electron microscopy. J Microsc 2011;241:179-87.
4. Hobley E, Willgoose GR, Frisia S, Jacobsen G. Vertical distribution of charcoal in a sandy soil: Evidence from DRIFT spectra and field emission scanning electron microscopy. Eur J Soil Sci 2014;65:751-62.
5. Cerqueira B, Arenas Lago D, Andrade ML, Vega FA. Using time of flight secondary ion mass spectrometry and field emission scanning electron microscopy with energy dispersive X ray spectroscopy to determine the role of soil components in competitive copper and cadmium migration and fixation in soils. Geoderma 2015;251 252:65 77. DOI: 10.1016/j.geoderma.2015.03.026.
6. Wang Y, Zhu Y, Chen S, Li W. Characteristics of the nanoscale pore structure in northwestern Hunan shale gas reservoirs using field emission scanning electron microscopy, high pressure mercury intrusion, and gas adsorption. Energy Fuels 2014;28:945-55. DOI: 10.1021/ef402159e.
7. Kutchko BG, Goodman AL, Rosenbaum E, Natesakhawat S, Wagner K. Characterization of coal before and after supercritical CO2 exposure via feature relocation using field-emission scanning electron microscopy. Fuel 2013;107:777-86.
8. Havrdova M, Polakova K, Skopalik J, Vujtek M, Mokdad A, Homolkova M, *et al*. Field emission scanning electron microscopy (FE-SEM) as an approach for nanoparticle detection inside cells. Micron 2014;67:149-54.
9. Wang X, Summers CJ, Wang ZL. Large-scale hexagonal-patterned growth of aligned ZnO nanorods for nano-optoelectronics and nanosensor arrays. Nano Lett 2004;4:423-6.
10. Sinha SK, Nair KG, Tyagi AK. Improvement in oxidation resistance of IMI834: Comparison between implantation and coating; a quest. Macromol Symp 2015;347:58-67.
11. Zhang R, Li H, Zhang ZD, Wang ZS, Zhou SY, Wang Z, *et al*. Graphene synthesis on SiC: Reduced graphitization temperature by C-cluster and Ar-ion implantation. Nucl Instrum Methods Phys Res B 2015;356-357:99-102.
12. Shikha D, Jha U, Sinha SK, Nair KG, Tyagi AK. Nitrogen ion beam modification of alumina for hard tissue implants. Macromol Symp 2015;347:39-48.
13. Shen Y, Qiao Y, He Z, Yu S. Enhancing electrical conductivity and electron field emission property of free standing diamond films by employing embedded Ag nanoparticles. Mater Lett 2015;139:322-4.
14. Eichelbaum M, Schmidt BE, Ibrahim H, Rademann K. Three-photon-induced luminescence of gold nanoparticles embedded in and located on the surface of glassy nanolayers. Nanotechnology 2007;18:355702.
15. Sharp ID, Xu Q, Yi DO, Yuan CW, Beeman JW, Yu KM, *et al*. Structural properties of Ge nanocrystals embedded in sapphire. J Appl Phys 2006;100:114317.
16. Wang Y, Liu XP, Qin GW. Transmission electron microscopy study of high-dose iron-implanted sapphire. Mater Charact 2015;102:19-23.
17. Gandman M, Ridgway M, Gronsky R, Glaeser AM. Microstructural evolution in Pt-implanted polycrystalline Al2O3. Acta Mater 2015;83:169-79.
18. Shemukhin AA, Nazarov AV, Balakshin YV, Chernysh VS. Defect formation and recrystallization in the silicon on sapphire films under Si+irradiation. Nucl Instrum Methods Phys Res B 2015;354:274-6.
19. Sánchez Dena O, Mota Santiago PE, Tamayo Rivera L, García Ramírez EV, Crespo-Sosa A, Oliver A, Reyes-Esqueda JA. Size and shape dependent nonlinear optical response of Au nanoparticles embedded in sapphire. Opt Mater Express 2014;4:1647 9. DOI: 10.1364/OME.4.000092
20. Mota Santiago PE, Crespo Sosa A, Jiménez Hernández JL, Silva Pereyra HG, Reyes Esqueda JA, Oliver A. Size characterisation of noble metal nano crystals formed in sapphire by ion irradiation and

subsequent thermal annealing. Appl Surf Sci 2012;259:574-81.
21. Niedrig H. Electron backscattering from thin films. J Appl Phys 1982;53:R15-49.
22. Lloyd GE. Atomic number and crystallographic contrast images with the SEM : A review of backscattered electron techniques. Mineral Mag 1987;51:3-19.
23. Isabell TC, Dravid VP. Resolution and sensitivity of electron backscattered diffraction in a cold field emission gun SEM. Ultramicroscopy 1997;67:59-68.
24. Kirk TL, Scholder O, De Pietro LG, Ramsperger U, Pescia D. Evidence of nonplanar field emission via secondary electron detection in near field emission scanning electron microscopy. Appl Phys Lett 2009;94:92-5.
25. Kim H, Negishi T, Kudo M, Takei H, Yasuda K. Quantitative backscattered electron imaging of field emission scanning electron microscopy for discrimination of nano-scale elements with nm-order spatial resolution. J Electron Microsc 2010;59:379-85.
26. Ziegler JF, Ziegler MD, Biersack JP. SRIM – The stopping and range of ions in matter (2010). Nucl Instrum Methods Phys Res B 2010;268:1818-23.
27. D'Orléans C, Stoquert J, Estournès C, Cerruti C, Grob J, Guille J, *et al*. Anisotropy of Co nanoparticles induced by swift heavy ions. Phys Rev B 2003;67:10-3.
28. Sosa IO, Noguez C, Barrera RG. Optical properties of metal nanoparticles with arbitrary shapes. J Phys Chem B 2003;107:6269-75.
29. Zhang JZ, Noguez C. Plasmonic optical properties and applications of metal nanostructures. Plasmonics 2008;3:127-50.
30. Gonzalez AL, Reyes-Esqueda JA, Noguez C. Optical properties of elongated noble metal nanoparticles. J Phys Chem C 2008;112:7356-62.
31. Sun Y, Xia Y. Shape-controlled synthesis of gold and silver nanoparticles. Science 2013;2176:2176-80.
32. Bykkam S, Ahmadipour M, Narisngam S, Kalagadda VR, Chidurala SC. Extensive studies on X-ray diffraction of green synthesized silver nanoparticles. Adv Nanoparticles 2015;4:1-10.
33. Schou J. Transport theory for kinetic emission of secondary electrons from solids by electron and ion bombardment. Nucl Instrum Methods 1980;170:317-20.
34. Can-Uc B, Rangel-Rojo R, Peña-Ramírez A, de Araújo CB, Baltar HT, Crespo-Sosa A, *et al.* Nonlinear optical response of platinum nanoparticles and platinum ions embedded in sapphire. Opt Express 2016;24:9955-65.

Microscopy Study, Structural and Optical Properties Correlated with the Morphology of Metallic Nanoparticles Embedded in Synthetic Sapphire

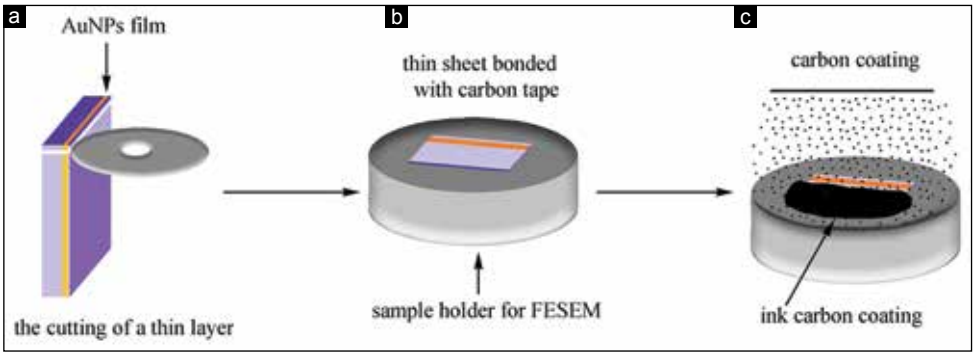

Figure SI1: Schematic methodology for sample preparation of GNPs embedded in a dielectric matrix in order to be observed in a JEOL FE-SEM 7800

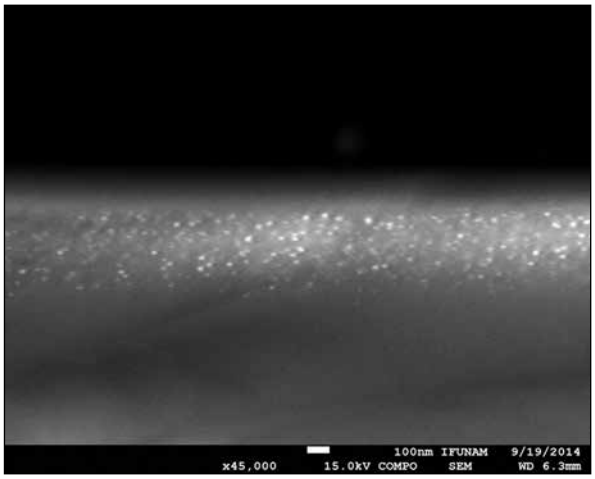

Figure SI2: Typical FESEM micrograph using backscattered electrons of metallic nanoparticles embedded in sapphire matrix, observed in transversal view without carbon layer

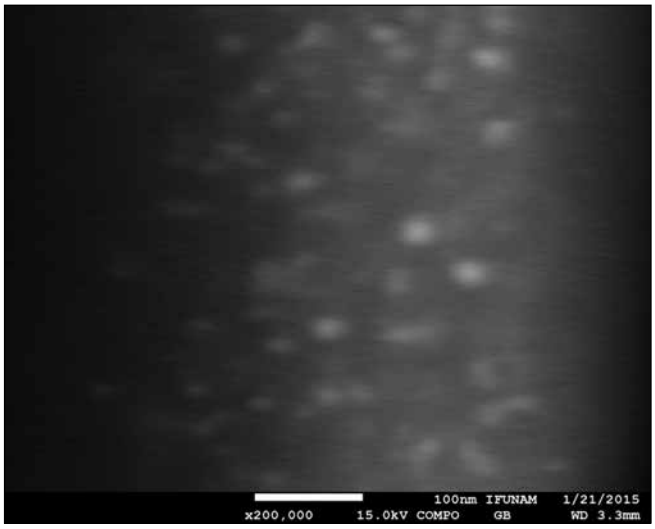

Figure SI3: Movement of the sample while capturing micrographs. Main charge effects observed during analysis in FESEM of samples produced by ion implantation

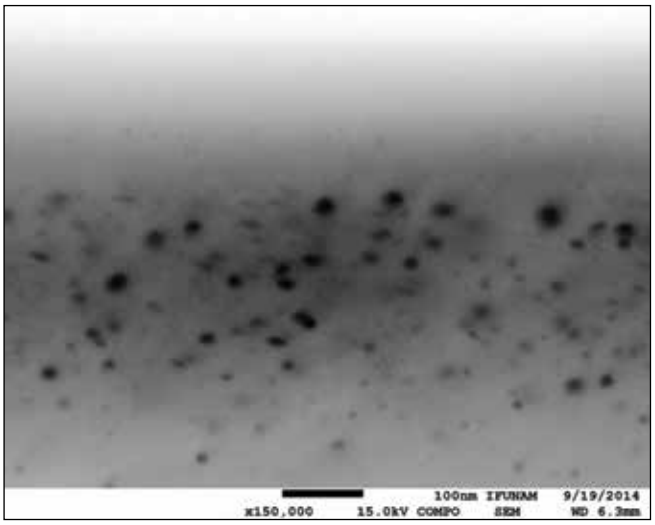

Figure SI4: Effect by the size of specimen: the thin layer of dielectric reduces the charge effects. Complete piece of sample

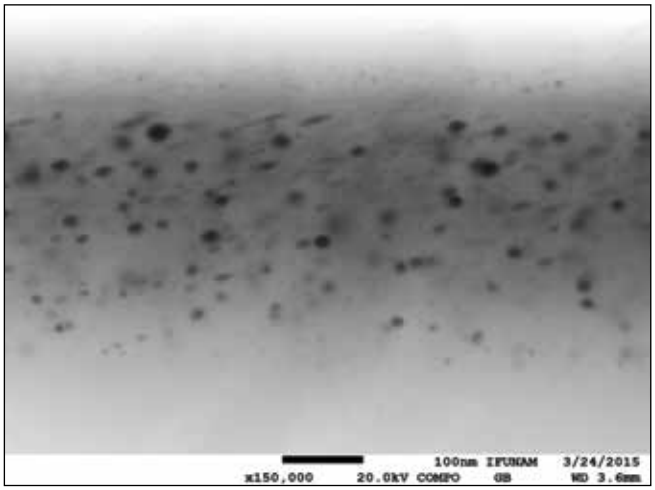

Figure SI5: Effect by the size of specimen: the thin layer of dielectric reduces the charge effects. Using a thin layer of carbon coating (10-15 nm)

Figure SI6: Total charge of the sapphire surface when observing the surface, catching the inner part of microscopy (mirror behavior of sapphire)

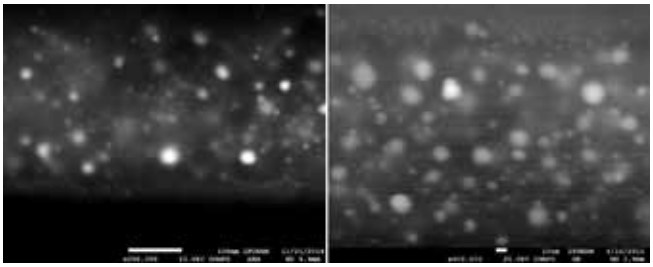

Figure SI7: Charging around around individual nanoparticles